sustainability

Article

Changes of Water Vapor Budget over East Asia in Response to $4xCO_2$ Concentration Forcing

Zhengqin Shen, Tao Xu, Guanyu Liu, Xuguang Sun * and Xiu-Qun Yang

China Meteorological Administration Key Laboratory for Climate Prediction Studies, School of Atmospheric Sciences, Nanjing University, Nanjing 210023, China
* Correspondence: xgsun@nju.edu.cn

Abstract: Water resources are essential for the economic development and social security in East Asia, especially under global warming. Based on newly released CMIP6 149-year simulation data from a pre-industrial control experiment (piControl) and a forced experiment on the abrupt quadrupling of CO_2 concentration (abrupt-$4xCO_2$), changes of water vapor budget over East Asia due to $4xCO_2$ concentration forcing and their possible mechanisms are investigated. Change of precipitation (P) demonstrates a spatial pattern of "Southern Flood and Northern Drought" (SFND) in eastern China, which can also be seen in the change of evaporation (E), though at a much smaller amplitude. The change of water vapor budget represented by E–P is dominated by P, which is primarily induced by changes of water vapor divergence associated with both moisture-related thermodynamic contribution and atmospheric circulation-related dynamic contribution. Specifically, under global warming, tropical El Nino-like SST warming causes weakened Walker circulation through decreased zonal temperature gradient, while amplified Arctic warming induces a negative Arctic Oscillation pattern via reduced meridional temperature gradient. The combined signals from tropical and mid-high latitudes result in significant long-term changes of water vapor convergence as well as much more precipitation in the Yangtze River Valley, forming the SFND. Furthermore, the intensity of the SFND change pattern could also have notable interdecadal variation, which is mainly attributed to the modulation of interdecadal signals of the Indian Ocean basin mode (IOBM) and Pacific Decadal Oscillation (PDO). Results of this study could provide an important scientific basis for the future planning and management of water resources over East Asia, specifically in eastern China.

Keywords: water vapor budget; $4xCO_2$ concentration forcing; Southern Flood and Northern Drought; El Nino-like SST warming; Walker circulation; amplified Arctic warming; Arctic Oscillation

Citation: Shen, Z.; Xu, T.; Liu, G.; Sun, X.; Yang, X.-Q. Changes of Water Vapor Budget over East Asia in Response to $4xCO_2$ Concentration Forcing. *Sustainability* **2023**, *15*, 313. https://doi.org/10.3390/su15010313

Academic Editor: Jan Hopmans

Received: 13 November 2022
Revised: 18 December 2022
Accepted: 22 December 2022
Published: 25 December 2022

1. Introduction

Water vapor budget (evaporation minus precipitation, abbr. E–P) has a decisive effect on the spatial and temporal distribution of water resources and its changes can exert an important impact on regional droughts and floods [1]. When it comes to the relationship between precipitation and divergence of water vapor flux, convergence of moisture is conductive to the generation of much more precipitation [2–6]. With regards to the effect of precipitation on water vapor, increasing evaporation and precipitation will accelerate the water cycle [7]. East Asia is densely populated and economically developed, and is also part of a typical global monsoon region. As one of the significant influencing factors of the intensity of the East Asia Summer monsoon (EASM), water vapor budget has a great effect on East Asian climate variability, extreme event forecasting and water resources. Understanding the mechanism behind the changes in water vapor budget and predicting these changes may have significant implications for the sustainable development of the economy and social society in East Asia within the context of global warming [1,7,8].

As the major dynamic component of water vapor transportation (WVT), EASM plays an important role in changes in the water vapor budget of East Asia. Changes of moisture advection caused by monsoon is the main reason for convergence and divergence of water vapor in summer [8,9]. In the context of global warming, the uneven temporal and spatial distributions of land and sea warming will cause significant changes in EASM. The EASM experienced an interdecadal weakening from the 1960s to the 1980s [9–11] associated with deficient rainfall in North China (NC) and excessive rainfall in the Yangtze River Valley (YRV) along 30° N; this is known as "Southern Flood and Northern Drought" (SFND) [12–16]. YRV and NC are prone to natural hazards from extreme weather events and have had six of the world's top ten deadliest floods of all time, attracting much attention in recent studies [17,18]. Meanwhile, the relatively dense population in these regions makes the floods much deadlier and costlier [19]. Model simulations and observations suggest that such precipitation patterns may be amplified by greater warming in the Arctic [20–22]. However, according to IPCC AR6, future precipitation is likely to increase in both winter and summer in NC, which will also elevate with the increase of CO_2 in different shared socioeconomic pathways (SSPs) [23]. CMIP5 projections indicate a likely rise in both the circulation and rainfall of the EASM throughout the 21st century. Correspondingly, the EASM has also begun to recover in recent decades [24,25]. According to some studies, under the background of global warming, precipitation in the Yangtze–Huaihe Valley will reduce while it will increase in high latitudes and in central China [25]. The discrepancies of previous studies suggest that the ways in which precipitation in YRV and NC will change under the circumstance of global warming is worthy of further analysis.

Change of water vapor content is also closely related to the change of temperature. In terms of global warming effects, some previous studies have directly used the Clausius–Clapeyron (C–C) equation to estimate the change of water vapor budget based on model results and obtained the spatial distribution change of "wet getting wetter and dry getting drier", wherein change rate of water vapor is about 7% per degree of Celsius [26,27]. However, although the projected E–P in CMIP3/IPCC AR4 models matches well with the prediction from the C–C equation, the projected change rate of water vapor is only 4% per degree Celsius, much less than the C–C-derived result, which means that some other factors must exist and have an influence over it [27]. While considering change of atmospheric circulation-related dynamic processes, change of precipitation can be entirely explained together with changes of humidity [27]. Additionally, in observations, there are also some uncertainties in the elements of water cycle on different time scales [28]. Therefore, how the water vapor changes under conditions of global warming needs to be further examined based on the updated model data. The moisture budget decomposition method is often used to estimate the relative contributions to rainfall changes from changes in atmospheric specific humidity (thermodynamic component) and circulation (dynamic component), however, these generally demonstrate large uncertainties and discrepancies among CMIP6 models under different warming scenarios [3–6].

In addition, most previous studies related to global warming have focused mainly on the long-term trends of temperature and precipitation, but their interdecadal variations may also have more practical importance to policy making, which may in turn modulate the effect of global warming. For example, the global surface warming hiatus is closely associated with the phase transitions of the Pacific Decadal Oscillation (PDO) and the Atlantic Multidecadal Oscillation (AMO) [29,30]. Zhang et al. [31] have pointed out that interdecadal changes of observed precipitation anomalies in East Asia can be determined by the phase combinations of PDO and AMO, together with the Indian Ocean basin warming mode (IOBM). Therefore, in this study, comparisons of the abrupt-4xCO_2 experiment and the piControl experiment from the state-of-the-art models in CMIP6 are made to illustrate the change of water vapor budget under global warming, wherein more focus is on the newest version of the Community Earth System Model (CESM). CESM2 has been shown to be better at climate simulation and prediction [32–35], including the related changes of precipitation over East Asia and their possible mechanisms. In addition, interdecadal modulation of PDO, AMO and IOBM on the intensity of the SFND change pattern is discussed as well.

2. Data and Methodology

2.1. CMIP6 Simulation Data

To investigate change of water vapor budget under global warming, output of piControl and abrupt-4xCO_2 experiments produced by CESM2 as well as other CMIP6 models were used in this study, both of whom belong to the Diagnostic, Evaluation and Characterization of Klima (DECK) experiments in CMIP6, which can be obtained freely at https://csegweb.cgd.ucar.edu/experiments/public. Compared with previous CMIP climate models, the most up-to-date CMIP6 models behave better in reproducing large-scale climate modes [36–38]. CESM2 is the newest version of CESM, and shows better performance in simulating the upper tropospheric velocity potential, jet streams and Arctic Oscillation (AO) [32–35], all of which have strong impacts on the East Asian monsoon [20,21]. PiControl in CMIP6 provides opportunities for an evaluation of the atmospheric model and the coupled system by establishing a baseline level. This is conducted under conditions chosen to be representative of the period before the onset of large-scale industrialization, with 1850 being the reference year with a fixed CO_2 concentration of 280 ppm. The idealized abrupt-4xCO_2 experiments in the DECK measure fundamental forcing and feedback response to extreme CO_2 increase, aiming at simulating climate sensitivity, feedback and response mechanisms. The CO_2 concentration in abrupt-4xCO_2 is immediately and abruptly quadrupled from the global annual mean 1850 value that is used in piControl [39,40], which is also more than twice the currently observed CO_2 concentration of around 420 ppm, indicating an extreme warming scenario without controlling CO_2 emissions. Due to the apparent features of precipitation difference between abrupt-4xCO_2 and piControl experiments during boreal summertime (June, July and August, JJA), we chose summertime from 1 to 149 model years as our study time period. In particular, the difference in the last 50 years of the study period (100–149 model years) between the two experiments was used to represent the effect of abnormal warming at a steady state.

2.2. Methodology

Vertical-integral WVT and its divergence are mainly used for water vapor budget analysis. Accordingly, vertical integrals of atmospheric water vapor (Q_{int}), atmospheric water vapor flux (WVF) (Q) and divergence of WVF (Q_{div}) are calculated as the following formulas [41,42]:

$$\boldsymbol{Q}_{\text{int}} = \frac{1}{\text{g}} \int_{p_l}^{p_s} q dp \tag{1}$$

$$\boldsymbol{Q} = \frac{1}{\text{g}} \int_{p_l}^{p_s} \mathbf{v} q dp \tag{2}$$

$$\boldsymbol{Q}_{div} = \nabla \cdot \boldsymbol{Q} = \frac{1}{\text{g}} \int_{p_l}^{p_s} \nabla \cdot \mathbf{v} q dp \tag{3}$$

where in q is specific humidity, v is wind velocity, and g is acceleration of gravity. All the integrals are from surface pressure p_s to upper-level pressure p_l, here, p_l is set to 300 hPa since water vapor is mostly concentrated below that level.

E–P is the source and sink term of water vapor in the atmosphere. Therefore, we have the equation for derivative of Q_{int} with time,

$$\frac{d\boldsymbol{Q}_{int}}{dt} = \rho_w g(E-P) = \frac{\partial \boldsymbol{Q}_{int}}{\partial \text{t}} + \boldsymbol{Q}_{div} \tag{4}$$

In a stable climate state, $\frac{\partial Q_{int}}{\partial \text{t}}$ is negligible, so the water vapor budget equation is diagnosed as follows [41]:

$$\rho_w g(E-P) = \int_0^{p_s} (\overline{\mathbf{v}} \cdot \nabla \overline{q} + \overline{q} \nabla \cdot \overline{\mathbf{v}}) dp + \int_0^{p_s} \nabla \cdot (\overline{q\prime \mathbf{v}\prime}) dp + q_s \mathbf{v}_s \cdot \nabla \mathbf{p}_s \tag{5}$$

Overbars indicate monthly means and primes indicate departures from the monthly mean, and the subscript s denotes surface values. E is evaporation, P is precipitation, ρ_w is density of water. More specifically, the first term at the right-hand side of equation (5) is the water vapor convergence by mean flow, and the second describes the transient eddies, while the last term involves surface quantities, having not been expressed as monthly and transient components respectively and separately.

Change of a variable due to the abrupt-4xCO_2 forcing against the pre-industrial CO_2 concentration is denoted by the following symbol,

$$\delta(\cdot) = (\cdot)_{4xCO_2} - (\cdot)_{pi} \tag{6}$$

In this equation, subscripts 4xCO_2 and pi indicate variable values in parentheses in abrupt-4xCO_2 and piControl experiments, respectively. Therefore, Equation (4) can be further approximated as:

$$\rho_w g\delta(E-P) = \int_0^{p_s} (\nabla\cdot(\overline{q}_{pi}[\delta\overline{\mathbf{v}}]) + \nabla\cdot(\overline{\mathbf{v}}_{pi}[\delta\overline{q}]) + \nabla\cdot(\delta\overline{\mathbf{v}}\delta\overline{q}))dp + \int_0^{p_s} \nabla\cdot(\delta\overline{\mathbf{v}\prime q\prime})dp + \delta S \tag{7}$$

On the right-hand side of Equation (7), the first term with regards to change of $\overline{\mathbf{v}}$ but no change of $\overline{q}$ is named as the dynamic term δMCD, the second involving change of $\overline{q}$ but no change of $\overline{\mathbf{v}}$ is referred to as the thermodynamic term δTH, and the third is called the nonlinear term δNL because it is related to the product of changes of both $\overline{q}$ and $\overline{\mathbf{v}}$, and all the three terms are expressed as Equations (8)–(10), accordingly. The transient eddy term $\int_0^{p_s} \nabla\cdot(\delta\overline{\mathbf{v}\prime q\prime})dp$ and the surface term δS are both relatively smaller and can be neglected (figures not shown), which is consistent with previous studies [41]. Therefore, Equation (7) can be further rewritten as Equation (11), which shows that change of water vapor budget is mainly attributed to the dynamic term δMCD, the thermodynamic term δTH and the nonlinear term δNL.

$$\delta MCD = \int_0^{p_s} \nabla\cdot(\overline{q}_{pi}[\delta\overline{\mathbf{v}}])dp \tag{8}$$

$$\delta TH = \int_0^{p_s} \nabla\cdot(\overline{\mathbf{v}}_{pi}[\delta\overline{q}])dp \tag{9}$$

$$\delta NL = \int_0^{p_s} \nabla\cdot(\delta\overline{\mathbf{v}}\delta\overline{q})dp \tag{10}$$

$$\rho_w g\delta(E-P) \approx \delta MCD + \delta TH + \delta NL \tag{11}$$

To quantitively represent changes of water vapor budget and precipitation during different periods and make comparisons, we also calculated the relative changes of precipitation, evaporation and P–E as $\frac{\delta P}{P_{pi0}}$, $\frac{\delta E}{E_{pi0}}$ and $\frac{\delta(P-E)}{(P-E)_{pi0}}$, and the subscript $_{pi0}$ denotes the mean value of the first 30 years in the piControl experiment, which is used as the baseline similar to the climatical normal defined by the World Meteorological Organization. In addition, an 11-year running mean is applied to these above-mentioned change rates in order to clearly display their low-frequency variations such as interdecadal variabilities and long-term trend.

Similar to Zhang et al. [31], PDO, AMO and IOBM and their indices were identified and used to explain the interdecadal variation of the water vapor budget. In particular, the PDO index is defined as the second principal component (PC) of North Pacific (20°–70° N) sea surface temperature (SST) anomalies since the leading PC is the warming trend, indices of AMO and IOBM are indicated by the area-averaged SST anomalies over the North Atlantic basin (0–60° N, 80°–0° W) and the Indian Ocean basin (45° S–20° N, 30°–120° E), respectively. Wherein, SST anomalies are calculated by the difference of abrupt-4xCO_2 experiment minus piControl experiment, and are weighted by the cosine of latitude before being applied for the derivation of these indices. Furthermore, in order to demonstrate the interdecadal relationship of PDO, AMO and IOBM with precipitation, the linear trends are all removed from the relevant indices.

3. Results

3.1. Changes of Precipitation, Evaporation and Water Vapor

Contrary to E–P, P–E represents the sink of water vapor, which means that the region will be more humid and wetter when it is positive. As shown in Figure 1a, in the piControl experiment, climatological precipitation is much larger in southern East Asia, especially from central China to the south of Japan, forming the Meiyu–Changma–Baiu (MCB) rain band. This is the defining feature of the East Asian summer climate [43,44], corresponding to the observation shown in a previous study [42], which indicates that the CESM2 model has good performance in simulating precipitation spatial characteristics over East Asia. Compared to the piControl experiment, precipitation in the abrupt-4xCO_2 experiment is significantly increased from the eastern Tibetan Plateau to the south of Japan through the YRV and South Korea, so that MCB precipitation will be greatly enhanced under global warming. In contrast, there is an obvious decreasing tendency of precipitation in NC. Wherein, YRV (100° E–120° E, 25° N–35° N) and NC (100° E–115° E, 35° N–45° N) are the two regions with the most prominent precipitation anomalies in eastern China, which forms a typical SFND pattern of changed precipitation there, consistent with the general findings that wetter regions get wetter while drier regions become drier [26]. However, different from the CMIP5 results, the center of reduced precipitation in northern China is mainly confined to the inland (Figure 1a), similar to the trend of observed precipitation anomalies during the period of 1961–2006 [45] (IPCC 2013). Furthermore, due to the abrupt-4xCO_2 forcing, precipitation is significantly decreased in the subtropical regions from the Indian summer monsoon region to the western North Pacific, especially around the western coasts of the Indian and Indo-China Peninsulas (Figure 1a).

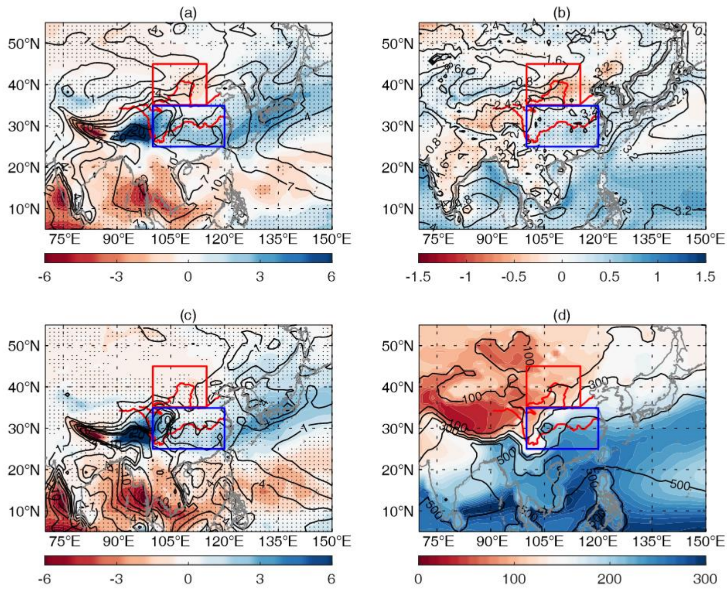

Figure 1. Changes of (**a**) precipitation, (**b**) evaporation and (**c**) P–E (unit: mm/day) and (**d**) Q_{int} (unit: $10g/g^*kg/m^2$) in JJA of 100–149 model years from piControl to abrupt-4xCO_2. Wherein the contour lines represent the climatology in the piControl experiment, and the colors are the differences of abrupt-4xCO_2 minus piControl. Dotted areas in (**a**–**c**) indicate the significance level of 0.05, and changes in (**d**) all pass the test of significance level of 0.05 in the study area. Red and blue boxes are the selected regions for North China and the Yangtze River Valley, respectively.

As for the evaporation, its climatological distribution over East Asia in the piControl experiment is similar to that of precipitation, but with a much smaller magnitude, as is the distribution of evaporation change, albeit significant at a 95% confidence level (Figure 1b), which is also well in agreement with other observations [46]. Considering the warming trend of low-level air temperature that demonstrates a generally meridional increase in the northern hemisphere (Figure 2b), a change of evaporation does not have to conform to the spatial distribution of change of temperature over East Asia, and instead could be mainly attributed to the change of soil moisture associated with a change of precipitation (Figure 1a). On the other hand, in the subtropical ocean regions, such as the Arabian Sea, Bay of Bengal and western North Pacific, evaporation is significantly increased (Figure 1b), which may be closely related to the local atmospheric warming (Figure 2b).

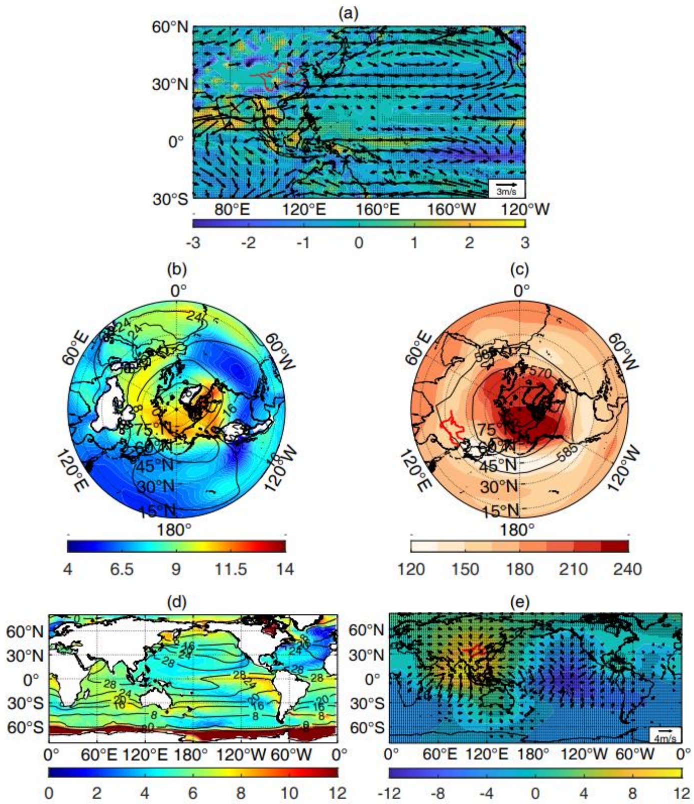

Figure 2. Similar to Figure 1 but for (**a**) 850hPa wind vector (unit: m/s) and its divergence (unit: 10^{-6}*s^{-1}), (**b**) 850hPa air temperature (unit: °C), (**c**) 500hPa geopotential height (unit: 10 gpm), (**d**) sea surface temperature (unit: °C), (**e**) 200hPa velocity potential (unit: m^{-1}*s^{-1}) and divergent wind vector (unit: m*s^{-1}). Changes in (**b**–**d**) all pass the test of significance level of 0.05.

Over East Asia, both climatological mean and climate change of P–E are dominated by the change of precipitation, especially for the major characteristics of SFND in change of P–E (Figure 1a,c), because the magnitude of precipitation change is much larger than that of evaporation change. In the subtropical region, changes of both decreased precipitation and increased evaporation lead to a significant decreasing change of P–E (Figure 1c), implying a relatively consistent relationship of precipitation and water vapor content there [20].

As shown in Figure 1d, climatological vertical-integral water vapor in the piControl experiment is much larger in the tropical regions, especially in the ocean, and it gradually decreases from southeast to northwest over East Asia. Change of vertical-integral water vapor over East Asia has a similar spatial pattern as its climatology in piControl experiment, is positive for all the study regions and is consistent with the increasing low-level air temperature according to the C–C equation (Figure 2b), which means that water vapor content is getting much larger under global warming. However, contrary to the uniform change of low-level air temperature, change of vertical-integral water vapor shows an obvious spatial pattern with more water vapor in coastal regions than in inland regions. Specifically, there is larger increase of water vapor in YRV than in NC. This pattern resembles the distribution of SFND in changes of both precipitation and P–E (Figure 1a,c), indicating the importance of water vapor to precipitation over East Asia.

3.2. Diagnosis of Water Vapor Budget

According to Equations (4) and (7), changes of water vapor and P–E are mainly dependent on the divergence of WVF. As shown in Figure 3a, with the exception of the WVF divergence change in the southern South China, a change of vertical-integral WVF divergence is closely consistent with P–E (Figures 1c and 3a), i.e., significant changes of convergence and divergence are located in YRV and in NC, respectively. The WVF convergence change along the YRV is caused by the change of WVT from both southwest and northwest directions, wherein the northwest water vapor flux brings cold dry air from high latitudes and the southwest water vapor flux mainly originates in South Asia and conveys tremendous warm moisture into the YRV, which may be highly related to the enhanced South Asian summer monsoon.

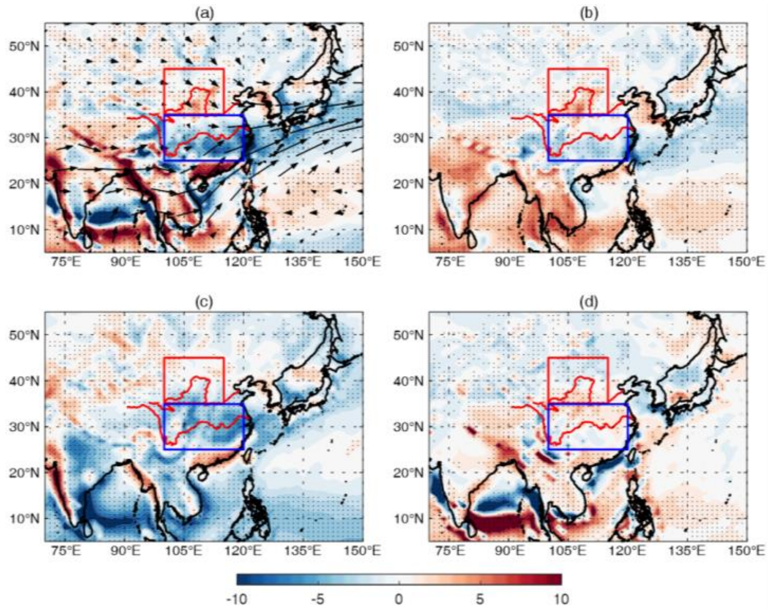

Figure 3. Similar to Figure 1 but for (**a**) Q (arrows, unit: g/g*kg/m^2*m/s) and Q_{div} (color, unit: 10^{-3}*g/g*kg/m^2*m/s*m^{-1}), and (**b**) δMCD, (**c**) δTH and (**d**) δNL (unit: 10^{-3}*g/g*kg/m^2*m/s*m^{-1}).

In order to further figure out the specific process of water cycle and water vapor budget over East Asia, the change of WVF divergence is further decomposed into three terms as shown in Equation (11), i.e., contributions of dynamic term δMCD, thermodynamic term δTH and nonlinear term δNL. Because of the change of wind vector (Equation (8)), δMCD induces significant WVF convergence change along the YRV and WVF divergence change in NC, especially in the Hetao region around the middle reaches of the Yellow River (Figure 3b), favoring SFND pattern in P–E (Figure 1c). As for the contribution of δTH (Equation (9)), it causes significant WVF convergence change over almost the whole of East Asia (Figure 3c), corresponding to the increasing change of water vapor (Figure 1d). Compared with δMCD, δTH is remarkable with larger amplitude along the YRV (Figure 3b,c), indicating that the δTH associated with increased water vapor is more essential for the water vapor budget and with much more precipitation there. However, in NC, δTH is contrary to δMCD and to the change of total water vapor budget as well, playing an offset role instead. Distribution pattern of WVF divergence change related to the δNL is more like the δMCD, but it has a much smaller amplitude along the YRV and a comparable amplitude in NC, which indicates that simultaneous changes of both wind vector and water vapor have negligible (great) influences on the water vapor budget along the YRV (NC).

3.3. Changes of Atmospheric Circulations

Since δMCD mainly determines the spatial pattern of change of water vapor budget, changes of atmospheric circulations were further examined to find out their potential sources. Figure 2a indicates that there is an obvious low-level wind convergence change along the YRV, which is generated by the anomalous northwest and southwest wind vectors at 850 hPa and consistent with the change of WVF over there. Wherein, the anomalous northwest wind is the western part of the anomalous basin-scale low-level cyclone circulation over the North Pacific, while the anomalous southwest wind is the outflow of the anomalous large-scale strong anticyclone circulation over the Bay of Bengal and South China Sea, which indicates the extension of an enhanced South Asian summer monsoon (SASM). Furthermore, because of such a strong anticyclone anomaly, most SASM regions are covered by the anomalous low-level divergence except for the southern and northern Indian peninsula. This is in accordance with the local negative δMCD (Figure 3b) and is responsible for the decrease in precipitation (Figure 1a) and the water vapor sink (Figure 1c) there.

In response to the abrupt-4xCO_2 forcing, 850 hPa temperature rises dramatically in the whole northern hemisphere, and its amplitude increases from the tropical region to the Arctic region, with the least warming of no less than 4 °C at the lower latitudes and the largest warming of more than 10 °C around the Arctic Circle (Figure 2b). This features the Arctic amplification as found in previous observations [47,48] but with a much larger amplitude. The significantly simulated warming in the Arctic region may be primarily related to the almost ice-free surface in the Arctic Ocean (Figure not shown). The meridional heterogeneous atmospheric warming could result in an uneven rise of geopotential height at 500 hPa, which demonstrates a negative AO pattern with much higher geopotential height in the Arctic (Figure 2c). It has been pointed that the Arctic's warming could suppress the EASM and increase precipitation over the YRV [49,50]. Furthermore, the relatively lower geopotential height anomaly in the mid-latitude North Pacific is rather distinctive, and is closely connected to the local basin-scale low-level cyclone anomaly (Figure 2a), displaying an equivalent quasi-barotropic structure.

In the tropical oceans, SST is also greatly warmed due to the abrupt-4xCO_2 forcing, featuring an El Nino-like SST warming, and has the least warming of around 4 °C in the eastern tropical Indian Ocean and western tropical Pacific and the largest warming of about 8 °C in the eastern Pacific cold tongue, forming a strong zonal SST gradient anomaly in the tropics (Figure 2d), which can also be seen in other models under global warming [51,52]. Such zonally uneven SST warming enhances and suppresses the convective activities in the central tropical Pacific and eastern tropical Indian Ocean, respectively, and is characterized by the significant divergence change over the central tropical Pacific and convergence change over the Bay of Bengal in the upper troposphere (Figure 2e), thus the Walker circulation is greatly weakened. The significantly reduced convective activity in the Bay of Bengal generates a Gill-type atmospheric response [53], i.e., a pair of symmetric anticyclone anomalies located in the off-equatorial Indian Ocean (Figure 2a). In turn, the anticyclone anomaly in the Bay of Bengal may enhance the SASM and shift it northward, which could further transport more sufficient water vapor from the Bay of Bengal to the YRV (Figure 3a). Together with the anomalous northwest wind induced by the basin-scale cyclone anomaly in mid-latitude North Pacific, the anomalous southwest wind associated with the anticyclone anomaly in the Bay of Bengal also produces significant changes of WVF convergence (Figure 3a) and water vapor budget (Figure 1c) in the YRV, finally contributing to the SFND pattern in eastern China (Figure 1a).

3.4. Interdecadal Change of Water Vapor Budget

As shown in Figure 4, change of water vapor budget associated with the SFND pattern also has obvious interdecadal variations during the whole study period. In YRV, change rate of precipitation is always positive and has an obvious increasing trend accompanied by large interdecadal variabilities along with time, whereas it is mainly negative and dominated by the interdecadal variation in NC. Change rate of evaporation is much smaller compared to the precipitation in YRV, and it generally shows an increasing trend as well, so the change rate of water vapor budget is determined by the precipitation there. However, in NC, change rate of evaporation is comparable and similar to that of precipitation albeit with relatively smaller amplitude. Furthermore, change rate of water vapor budget also features interdecadal variabilities rather than a long-term trend under the constant 4xCO_2 concentration forcing. Compared with the evolvements of change rates of precipitation and water vapor budget in YRV and NC, it is clear to see that they are basically out of phase for both long-term trend and interdecadal variation (Figure 4). This means that the SFND pattern in eastern China may be still the typical pattern under global warming.

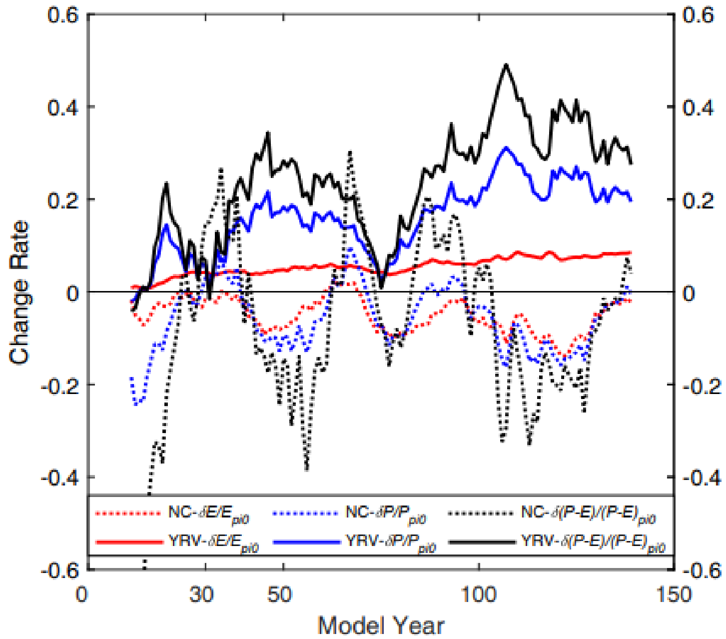

Figure 4. Evolvements of change rates in evaporation (δE, red), precipitation (δP, blue), and the difference between them (δ(P–E), black) in YRV (solid line) and NC (dash line) against their corresponding mean of the first 30 years of the piControl experiment. All are smoothed with an 11-year running mean.

Zhang et al. [31] have pointed out that the interdecadal variation of precipitation in East Asia is controlled by the joint modulation effect of PDO, AMO and IOBM [28]. Associated with the change of precipitation as the SFND pattern due to abrupt-4xCO_2 forcing, PDO index displays an obvious interdecadal variability (Figure 5a), whereas indices of AMO (Figure 5b) and IOBM (Figure 5c) are more like an increasing trend, especially for the IOBM index, which is responsible for the typical SFND pattern of the long-term trend of precipitation change [31]. When PDO, AMO and IOBM indices are detrended they all show notable interdecadal variabilities (Figure 5d), and PDO is strongly positively correlated with IOBM (0.59) but negatively correlated with AMO (−0.46), wherein the out-of-phase relationship between PDO and AMO under global warming is consistent with observations during the recent 100 years [31,54]. At the interdecadal time scale, changes of precipitation in YRV and NC are negatively correlated with each other (−0.35) (Figure 5e), wherein, change of precipitation in YRV is significantly positively correlated with the IOBM (0.43) but has no relations with AMO (0.02). On the contrary, change of precipitation in NC is most related to PDO with negative correlation (−0.34), followed by IOBM (−0.25) and AMO (0.24) in turn. Therefore, the impact factors on the changes of precipitation in YRV and NC are a little different, nevertheless, their combinations provide a possible explanation for the interdecadal change of the SFND pattern and further modulate the long-term trend under global warming.

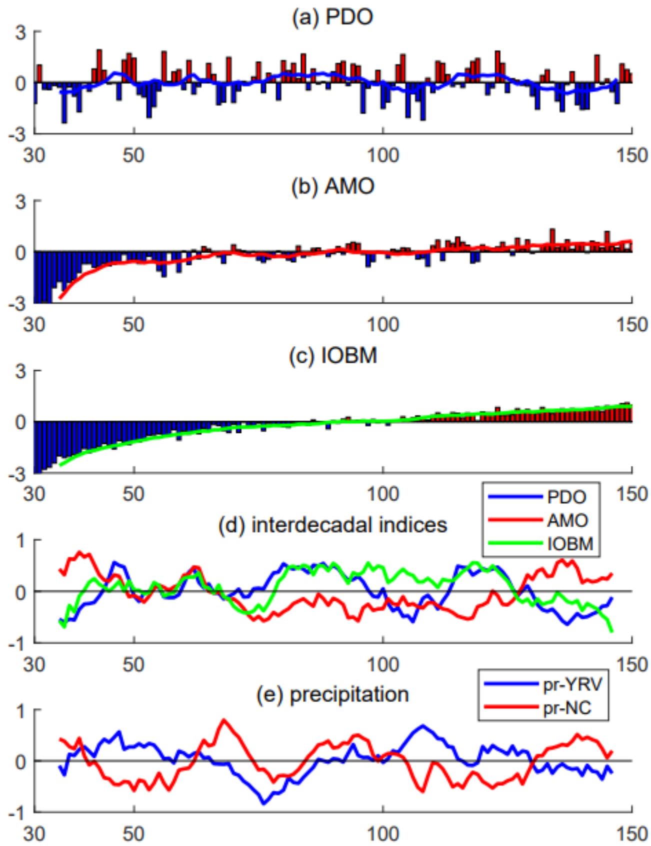

Figure 5. Detrended and standardized indices of (**a**) PDO (blue), (**b**) AMO (red), (**c**) IOBM (green) (filled bars) together with their 11-yr running means (colored thick lines), and (**d**) the overlap of their smoothed indices. (**e**) Detrended and standardized area-averaged precipitation in YRV (blue) and NC (red).

3.5. Comparison with Multi-Model Results

To further verify and confirm the above results from CESM2, changes of precipitation, geopotential height at 500 hPa and WVF in JJA from piControl to abrupt-4xCO_2 from the other 28 CMIP6 models as well as the multi-model ensemble (MME) mean with the total of 29 CMIP6 models including CESM2 were also calculated, and were further compared to those in CESM by pattern correlation (Figure 6a).

As suggested by the IPCC Third Assessment Report—Climate Change 2001 [55], the pattern correlation coefficients should be computed directly without computing anomalies from a central mean to represent climate change. As shown in Figures 7a and S1, 20 models and MME show a similar spatial distribution of precipitation change to CESM2 (passing the significance test at the level of 0.05), except for very few CMIP6 models, such as MIROC-ES2L, FGOALS-g3, MIROC6 (Figure 6a). To further show the representative of the pattern correlation coefficient and the change of SFND pattern in different models, we defined an SFND index, which is calculated as the difference of area-averaged precipitation anomalies between YRV and NC and then standardized by the variance of precipitation anomaly over eastern China (25° N–45° N, 105° E–120° E). A comparison of pattern correlation coefficient and SFND index shows that most models with positive pattern correlation coefficient illustrate an increasing SFND index as CESM2 except for BCC-ESM1 and CAMS-CSM1-0, and vice versa (Figure 6). In terms of WVF, most of the models, including the MME, indicate an enhanced southwest WVF, which brings a large amount of warm moisture into the YRV along with the strengthened South Asian summer monsoon as Section 3.2 elucidated (Figures 7b and S2). As for the geopotential height at 500 hPa in the northern hemisphere, although the changing magnitudes are different, all the models show significantly lifted geopotential height. Nineteen of 29, as well as the MME, show the pattern of negative phase of AO with higher increase in the Arctic and a lower increase in the mid-latitudes, especially over the North Pacific (Figures 7c and S3). At the same time, Figures 7d and S4 show that almost all the CMIP6 models, including the MME, feature an El Nino-like SST warming in the tropical Pacific Ocean.

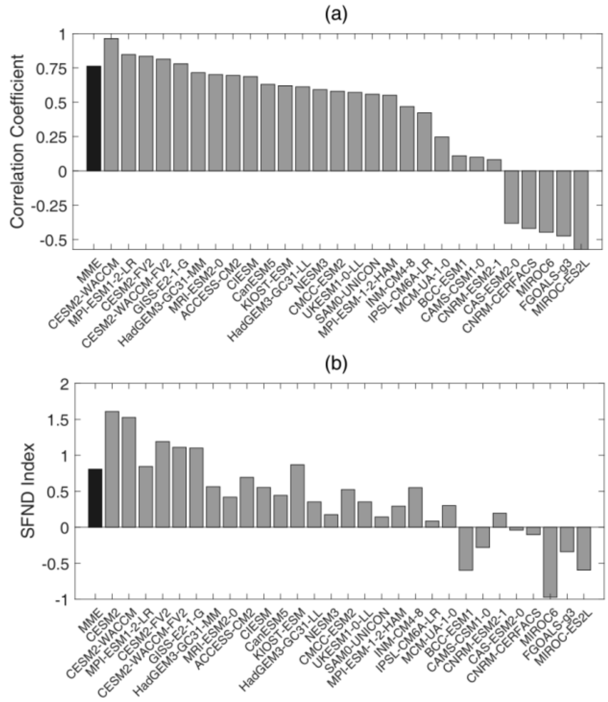

Figure 6. (**a**) Pattern correlation between the changes (with the same analysis as in CESM2) of precipitation in each model including MME. The calculated regions are 25° N–45° N, 105° E–120° E. (**b**) SFND Index defined as the standardized difference of precipitation between YRV and NC. The dark bar indicates the MME, and the other gray bars indicate the 28 (29) individual CMIP6 models excluding (including) the CESM2 in (**a**) (in (**b**)).

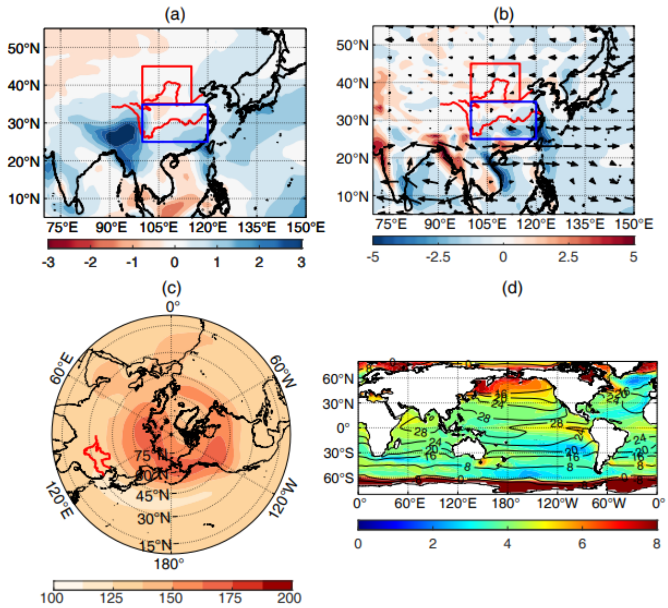

Figure 7. Changes of (**a**) precipitation (unit: mm/day), (**b**) 500hPa geopotential height (unit: 10 gpm), (**c**) water vapor flux Q (arrows, unit: g/g*kg/m^2*m/s) and Q_{div} (color, unit: 10^{-3}*g/g*kg/m^2*m/s*m^{-1}) in MME and (**d**) sea surface temperature (unit: °C).

In terms of the high similarities in water vapor budget and related atmospheric circulation and SST changes between CESM2 and MME (Figures 1, 2 and 7), the associated mechanism for the change of water vapor budget over East Asia in CESM2 also works in most of the other CMIP6 models of CMIP6. This further highlights the important joint contributions of El Nino-like SST warming in the tropical region and negative AO pattern in the mid-high latitudes under the extreme global warming due to the abrupt-4xCO_2 forcing.

4. Conclusions and Discussion

To reveal the change of water vapor budget, especially the precipitation over East Asia under global warming, the two latest CEMS2 experiments in CMIP6 such as piControl and abrupt-4xCO_2 were firstly used for detailed analysis in this study. This is because CESM2 has better performance in East Asia monsoon and dynamic processes [32–35], performances which were further verified and confirmed by most of the other CMIP6 models as well as the MME. We should note that although the SFND pattern obtained in MME is similar to that in CESM2 (Figures 1a and 7a), its intensity is rather weaker than that of CESM2 due to the offset effects of some models with opposite pattern (Figure 6b). Therefore, it is an appropriate way to demonstrate the results with both the credible model and the MME since over-reliance on the MME could lead to some confusing or uncertain results. The flowchart for the complete study is shown in Figure 8, and the main conclusions are as follows:

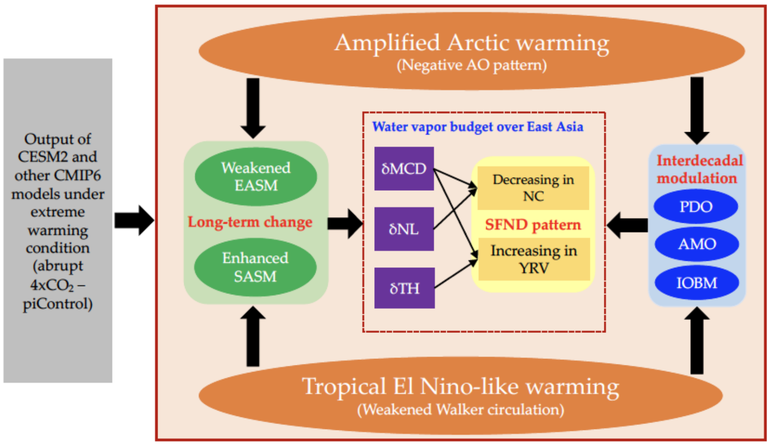

Figure 8. Schematic diagram summarizing the changes in water vapor budget and precipitation over East Asia as well as the related dynamical processes under extreme warming condition.

YRV and NC are the typical humid and dry inland regions over East Asia, respectively, where close relationships exist among vertical-integral water vapor, precipitation and evaporation. In response to global warming due to the abrupt-4xCO_2 forcing, vertical-integral water vapor in both regions increases significantly, and is more obvious in YRV than in NC, which corresponds to the spatial distribution characteristics of SFND pattern of precipitation change in eastern China. This is also consistent with the conclusion of "wet getting wetter and dry getting drier" proposed in previous studies [26]. Change of evaporation has basically the same spatial pattern with precipitation, but with obviously smaller amplitude. Changes of water vapor budget in YRV and NC are mainly determined by the convergence and divergence of WVF anomaly, respectively, and can be further decomposed into the atmospheric circulation-related dynamic term δMCD, the water vapor-related thermodynamic term δTH, and the combination of atmospheric circulation and water vapor-related nonlinear term δNL. In YRV, both δMCD and δTH could strengthen the convergence change of WVF, but δTH is much more essential. Whereas in NC, divergence change of WVF is predominately caused by δMCD and δNL, which is offset by δTH with convergence change of WVF to some extent.

Associated with the abrupt-4xCO_2 forcing induced global warming, changes of low-level atmospheric temperature in the northern hemisphere and tropical SST demonstrate uneven spatial warming distributions. The increasing meridional warming in low-level atmospheric temperature makes the Arctic the warmest region in the northern hemisphere, which in turn causes a negative AO pattern in change of 500 hPa geopotential height. Here, an equivalent quasi-barotropic low pressure structure over the mid-latitude North Pacific favors a strong basin-scale low-level cyclone anomaly, which produces an anomalous northwest wind over northeastern East Asia, bringing cold dry air to the YRV and increase the EASM-caused precipitation in YRV. At the same time, the relatively lesser SST warming in the eastern tropical Indian Ocean and western tropical Pacific and much larger SST warming in the eastern Pacific cold tongue feature an El Nino-like SST warming in the tropical region, which reduces the zonal SST gradient and weakens the Walker circulation. In turn, the convective activity in the Bay of Bengal is suppressed, and as the Gill-type atmospheric response, a strong low-level anticyclone is generated there. Thus, the South Asian summer monsoon is significantly enhanced and shifted northward, and can transport much more warm water vapor from the Bay of Bengal to the YRV. Therefore, the changes of atmospheric circulations from both the tropical region and mid-high latitudes cause the SFND pattern in eastern China.

It is also notable that in the CESM2 model, the intensity of the SFND change pattern together with changes of precipitation and water vapor budget have obvious interdecadal variations, though their phases remain the same during the study period. Additionally, those in YRV and NC are negatively correlated at the interdecadal time scale, which are further caused by the combined effect of PDO, AMO and IOBM [31]. In particular, IOBM and PDO play an essential role in the change of precipitation in YRV and NC, respectively. In other words, the interdecadal signals of PDO, AMO and IOBM might be modulated by global warming [56], and, in turn, they can further modulate the long-term trend of the SFND pattern under global warming. This makes its intensity stronger or weaker during some interdecadal periods, just as with their contributions to the global warming hiatus [29,30]. Therefore, we should take these interdecadal signals into account when we project future water resources under global warming.

The results of this study could provide an important scientific basis for the future planning and management of water resources over East Asia, especially in eastern China. However, it should be noted that the projected SFND pattern of future water vapor budget over East Asia in this study is different from some previous studies [23,24] that have argued that the major causes of the the intensified EASM and increased precipitation over northern China may reside in the atmospheric circulation changes in mid-high latitudes. This is because the enhanced northward transportation of warm moisture from the tropical region is generally consistent among different studies [23,24] (Figures 2 and 7). Because of the Arctic amplification under global warming, a negative AO pattern will form in mid-high latitudes [30,31] (Figures 2 and 7). Compared to the relatively smaller amplitude of global warming (such as 1.5 or 2.0 °C) [23,24], it is much larger due to the abrupt-4xCO_2 forcing, e.g., more than 5 °C in MME and more than 7 °C in CESM2 (Table 1). Thus, the negative AO could get much stronger and play a more important role in blocking the enhanced northward transportation of warm moisture, which eventually confines the water vapor convergence to the YRV and favors the SFND pattern. Therefore, how the water vapor budget over East Asia changes in different global warming scenarios may be greatly dependent on the atmospheric circulation responses in mid-high latitudes, and we should pay more attention to these in future.

The intensification of "South flooding and North drought" in eastern China due to the abrupt 4x increase in CO_2 concentrations has indeed great implications for guiding water resource planning, production and energy sectors. For water resource planning and production, such a precipitation anomaly distribution pattern indicates the urgency and necessity of constructing water conservancy infrastructure in China, such as "the South-to-North Water Diversion Project". This project can transfer the surplus water resources in the South to the arid North during periods of severe water shortage in China, realizing the recycling of floodwaters, which is of extra importance in the context of global warming, such as in the 4xCO_2 scenario [57,58]. It should also become an important task of water resources research and water conservancy construction in China at present and in the future. For energy sectors, this might shed light on the difference between the construction of new energy power generation facilities in the North and South of China. Specifically, in the future, more photovoltaic power generation should be built in the North due to the deficiency of precipitation, while more hydro-power facilities should be built in the South because of the increase of water resources.

Table 1. Information of the models and changes in mean global surface temperature in JJA of 100–149 model years from piControl to abrupt-4xCO_2.

Model Name	Institute	Atmospheric Resolution lon × lat		△T/°C
MME		\	\	5.4129
CESM2	NCAR (USA)	288	192	7.1264
CESM2-WACCM	NCAR (USA)	288	192	6.2819
MPI-ESM1-2-LR	MPI (Germany)	192	96	4.3695
CESM2-FV2	NCAR (USA)	144	96	5.3989
CESM2-WACCM-FV2	NCAR (USA)	144	96	5.1820
GISS-E2-1-G	NASA(USA)	144	90	3.9463
HadGEM3-GC31-MM	MOHC (UK)	432	325	7.4596
MRI-ESM2-0	MIROC (Japan)	320	160	4.5636
ACCESS-CM2	CSIRO (Australia)	192	145	6.4127
CIESM	THU(China)	288	192	7.7117
CanESM5	CCCMA(Canada)	128	64	7.4240
KIOST-ESM	KIOST(Korea)	192	96	4.2120
HadGEM3-GC31-LL	MOHC (UK)	192	145	7.5954
NESM3	NUIST(China)	192	96	6.4709
CMCC-ESM2	CMCC(Italy)	288	192	5.7749
UKESM1-0-LL	MOHC (UK)	192	145	7.3271
SAM0-UNICON	SNU(Korea)	288	192	4.0375
MPI-ESM-1-2-HAM	MPI-M(Germany)	192	96	3.6496
INM-CM4-8	INM(Russia)	180	120	3.3066
IPSL-CM6A-LR	IPSL(France)	144	143	6.9031
MCM-UA-1-0	UA(USA)	96	80	5.0268
BCC-ESM1	BCC(China)	128	64	4.6847
CAMS-CSM1-0	CAMS(China)	320	160	3.8605
CNRM-ESM2-1	CNRM(France)	256	128	5.9369
CAS-ESM2-0	CAS(China)	256	128	5.2790
CNRM-CERFACS	CNRM(France)	256	128	6.3996
MIROC6	MIROC (Japan)	256	128	3.6391
FGOALS-g3	CAS(China)	180	80	3.1859
MIROC-ES2L	MIROC (Japan)	128	64	3.8070

Supplementary Materials: The following supporting information can be downloaded at: https://www.mdpi.com/article/10.3390/su15010313/s1, Figure S1: Changes of precipitation in different models (including MME, unit: mm/day), figures are in the order of precipitation pattern correlation coefficients illustrated in Figure 5a; Figure S2: Similar to Figure S1 but for geopotential height (unit: 10 gpm); Figure S3: Similar to Figure S1 but for water vapor flux(arrows, unit: $g/g*kg/m^2*m/s$) and its convection (shadow, unit: $10^{-3}*g/g*kg/m^2*m/s*m^{-1}$); Figure S4: Similar to Figure S1 but for sea surface temperature (unit: °C).

Author Contributions: Z.S. produced the figures and wrote the manuscript. X.S. was responsible for the main idea of the manuscript and contributed to the manuscript revision. T.X., G.L. and Z.S. provided input to figures and text editing. X.-Q.Y. reviewed and provided text editing. All authors have read and agreed to the published version of the manuscript.

Funding: The National Key R&D Program of China (2022YFE0106600), the National Natural Science Foundation of China (Grant No. 41775074), the National Undergraduate Innovation and

Entrepreneurship Training Program of China (Grant No. 202010284156Z), the Foundation for Innovative Research Groups of the National Natural Science Foundation of China (Grant No. 41621005), and the Fundamental Research Funds for the Central Universities of China.

Institutional Review Board Statement: Not applicable.

Informed Consent Statement: Not applicable.

Data Availability Statement: Output of piControl and abrupt-4xCO_2 experiments produced by CMIP6 models belong to the Diagnostic, Evaluation and Characterization of Klima (DECK) experiments in CMIP6, which can be obtained freely at website https://csegweb.cgd.ucar.edu/experiments/public.

Acknowledgments: This study was jointly supported by the National Key R&D Program of China (2022YFE0106600), the National Natural Science Foundation of China (Grant No. 41775074), the National Undergraduate Innovation and Entrepreneurship Training Program of China (Grant No. 202010284156Z), the Foundation for Innovative Research Groups of the National Natural Science Foundation of China (Grant No. 41621005), and the Fundamental Research Funds for the Central Universities of China.

Conflicts of Interest: The authors declare no conflict of interest.

References

1. Muller, C.J.; Back, L.E.; O'Gorman, P.A.; Emanuel, K.A. A model for the relationship between tropical precipitation and column water vapor. *Geophys. Res. Lett.* **2009**, *36*, L16804. [CrossRef]
2. Betts, A.K. Coupling of water vapor convergence, clouds, precipitation, and land-surface processes. *J. Geophys. Res. Atmos.* **2007**, *112*, D10108. [CrossRef]
3. Chen, Z.; Zhou, T.; Zhang, L.; Chen, X.; Zhang, W.; Jiang, J. Global land monsoon precipitation changes in CMIP6 projections. *Geophys. Res. Lett.* **2020**, *47*, e2019GL086902. [CrossRef]
4. Li, Z.; Sun, Y.; Li, T.; Ding, Y.; Hu, T. Future changes in East Asian summer monsoon circulation and precipitation under 1.5 to 5 °C of warming. *Earths Future* **2019**, *7*, 1391–1406. [CrossRef]
5. Zhou, S.; Huang, G.; Huang, P. Changes in the East Asian summer monsoon rainfall under global warming: Moisture budget decompositions and the sources of uncertainty. *Climate Dyn.* **2018**, *51*, 1363–1373. [CrossRef]
6. Zhou, S.; Huang, G.; Huang, P. Inter-model spread of the changes in the East Asian summer monsoon system in CMIP5/6 models. *J. Geophys. Res. Atmos.* **2020**, *12*, 2020JD033016. [CrossRef]
7. Chou, C.; Neelin, J.D.; Chen, C.A.; Tu, J.Y. Evaluating the "Rich-Get-Richer" Mechanism in Tropical Precipitation Change under Global Warming. *J. Clim.* **2009**, *22*, 1982–2005. [CrossRef]
8. Huang, R.H.; Zhang, Z.Z.; Huang, G.; Ren, B.H. Characteristics of the Water Vapor Transport in East Asian Monsoon Region and Its Difference from that in South Asian Monsoon Region in Summer. *Chin. J. Atmos. Sci.* **1998**, *22*, 460–469.
9. Hori, M.E.; Nohara, D.; Tanaka, H.L. Influence of Arctic Oscillation towards the Northern Hemisphere surface temperature variability under the global warming scenario. *J. Meteor. Soc. Japan* **2007**, *85*, 847–859. [CrossRef]
10. Li, H.M.; Dai, A.G.; Zhou, T.J.; Lu, J. Responses of East Asian summer monsoon to historical SST and atmospheric forcing during 1950–2000. *Clim. Dyn.* **2010**, *34*, 501–514. [CrossRef]
11. Zhu, C.W.; Wang, B.; Qian, W.H.; Zhang, B. Recent weakening of northern East Asian summer monsoon: A possible response to global warming. *Geophys. Res. Lett.* **2012**, *39*, L09701. [CrossRef]
12. Gong, D.Y.; Ho, C.H. The Siberian High and climate change over middle to high latitude Asia. *Theor. Appl. Climatol.* **2002**, *72*, 1–9. [CrossRef]
13. Hu, Z.Z. Interdecadal variability of summer climate over East Asia and its association with 500 hPa height and global sea surface temperature. *J. Geophys. Res. Atmos.* **1997**, *102*, 19403–19412. [CrossRef]
14. Wang, J.; Gaffen, D.J. Trends in extremes of surface humidity, temperature, and summertime heat stress in China. *Adv. Atmos. Sci.* **2001**, *18*, 742–751. [CrossRef]
15. Yu, R.C.; Wang, B.; Zhou, T.J. Tropospheric cooling and summer monsoon weakening trend over East Asia. *Geophys. Res. Lett.* **2004**, *31*, L22212. [CrossRef]
16. Zhu, Y.; Yang, X. Relationships between pacific decadal oscillation (PDO) and climate variabilities in China. *J. Meteor. Res.* **2003**, *61*, 641–654.
17. Dore, M.H.I. Climate change and changes in global precipitation patterns: What do we know? *Environ. Int.* **2005**, *31*, 1167–1181. [CrossRef]
18. Zhang, L.X.; Zhou, T.J. Drought over East Asia: A Review. *J. Clim.* **2015**, *2*, 3375–3399. [CrossRef]
19. Jiang, T.; Shi, Y. Global climatic warming, the Yangtze floods and potential loss. *Adv. Earth Sci.* **2003**, *18*, 277–284.
20. Guo, D.; Gao, Y.Q.; Bethke, I.; Gong, D.Y.; Johannessen, O.M.; Wang, H.J. Mechanism on how the spring Arctic sea ice impacts the East Asian summer monsoon. *Theor. Appl. Climatol.* **2014**, *115*, 107–119. [CrossRef]

21. Wu, B.Y.; Zhang, R.H.; Wang, B.; D'Arrigo, R. On the association between spring Arctic sea ice concentration and Chinese summer rainfall. *Geophys. Res. Lett.* **2009**, *36*, L09501. [CrossRef]
22. Wu, B.Y.; Li, Z.K. Possible impacts of anomalous Arctic sea ice melting on summer atmosphere. *Int. J. Climatol.* **2022**, *42*, 1818–1827. [CrossRef]
23. IPCC. IPCC Sixth Assessment Report. Working Group 1: The Physical Science Basis. 2021. Available online: https://www.ipcc.ch/report/ar6/wg1/ (accessed on 15 December 2022).
24. Liu, H.W.; Zhou, T.J.; Zhu, Y.X.; Lin, Y.H. The strengthening East Asia summer monsoon since the early 1990s. *Chin. Sci. Bull.* **2012**, *57*, 1553–1558. [CrossRef]
25. Wang, T.; Miao, J.P.; Sun, J.Q.; Fu, Y.H. Intensified East Asian summer monsoon and associated precipitation mode shift under the 1.5 degrees C global warming target. *Adv. Clim. Chang. Res.* **2018**, *9*, 102–111. [CrossRef]
26. Zhou, T.J.; Yu, R.C.; Zhang, X.H.; Yu, Y.Q.; Li, W.; Liu, H.L.; Liu, X.Y. Features of Atmospheric Moisture Transport, Convergence and Air-Sea Freshwater Flux Simulated by the Coupled Climate Models. *Chin. J. Atmos. Sci.* **2001**, *25*, 596–608.
27. Held, I.M.; Soden, B.J. Robust responses of the hydrological cycle to global warming. *J. Clim.* **2006**, *19*, 5686–5699. [CrossRef]
28. Huntington, T.G. Evidence for intensification of the global water cycle: Review and synthesis. *J. Hydrol.* **2006**, *319*, 83–95. [CrossRef]
29. Dai, A.G.; Fyfe, J.C.; Xie, S.P.; Dai, X.G. Decadal modulation of global surface temperature by internal climate variability. *Nat. Clim. Change* **2015**, *5*, 555–559. [CrossRef]
30. Liu, W.; Xie, S.P. An Ocean View of the Global Surface Warming Hiatus. *Oceanography* **2018**, *31*, 72–79. [CrossRef]
31. Zhang, Z.Q.; Sun, X.G.; Yang, X.Q. Understanding the Interdecadal Variability of East Asian Summer Monsoon Precipitation: Joint Influence of Three Oceanic Signals. *J. Clim.* **2018**, *31*, 5485–5506. [CrossRef]
32. Danabasoglu, G.; Lamarque, J.F.; Bacmeister, J.; Bailey, D.A.; DuVivier, A.K.; Edwards, J.; Emmons, L.K.; Fasullo, J.; Garcia, R.; Gettelman, A.; et al. The Community Earth System Model Version 2 (CESM2). *J. Adv. Model. Earth Syst.* **2020**, *12*, MS001916. [CrossRef]
33. Ge, F.; Zhu, S.P.; Luo, H.L.; Zhi, X.F.; Wang, H. Future changes in precipitation extremes over Southeast Asia: Insights from CMIP6 multi-model ensemble. *Environ. Res. Lett.* **2021**, *16*, 024013. [CrossRef]
34. Ma, Y.L.; Yuan, N.M.; Dong, T.Y.; Dong, W.J. On the Pacific Decadal Oscillation Simulations in CMIP6 Models: A New Test-Bed from Climate Network Analysis. *Asia-Pac. J. Atmos. Sci.* 2022. Available online: https://link.springer.com/articledoi.org/10.1007/s13143-022-00286-1 (accessed on 18 August 2022).
35. Coburn, J.; Pryor, S.C. Differential credibility of climate modes in CMIP6. *J. Clim.* **2021**, *34*, 8145–8164. [CrossRef]
36. Ha, K.J.; Moon, S.; Timmermann, A.; Kim, D. Future Changes of Summer Monsoon Characteristics and Evaporative Demand Over Asia in CMIP6 Simulations. *Geophys. Res. Lett.* **2020**, *47*, GL087492. [CrossRef]
37. Jiang, D.B.; Hu, D.; Tian, Z.P.; Lang, X.M. Differences between CMIP6 and CMIP5 Models in Simulating Climate over China and the East Asian Monsoon. *Adv. Atmos. Sci.* **2020**, *37*, 1102–1118. [CrossRef]
38. Xin, X.G.; Wu, T.W.; Zhang, J.; Yao, J.C.; Fang, Y.J. Comparison of CMIP6 and CMIP5 simulations of precipitation in China and the East Asian summer monsoon. *Int. J. Climatol.* **2020**, *40*, 6423–6440. [CrossRef]
39. Eyring, V.; Bony, S.; Meehl, G.A.; Senior, C.A.; Stevens, B.; Stouffer, R.J.; Taylor, K.E. Overview of the Coupled Model Intercomparison Project Phase 6 (CMIP6) experimental design and organization. *Geosci. Model Dev.* **2016**, *9*, 1937–1958. [CrossRef]
40. Eyring, V.; Cox, P.M.; Flato, G.M.; Gleckler, P.J.; Abramowitz, G.; Caldwell, P.; Collins, W.D.; Gier, B.K.; Hall, A.D.; Hoffman, F.M.; et al. Taking climate model evaluation to the next level. *Nat. Clim. Change* **2019**, *9*, 102–110. [CrossRef]
41. Seager, R.; Naik, N.; Vecchi, G.A. Thermodynamic and Dynamic Mechanisms for Large-Scale Changes in the Hydrological Cycle in Response to Global Warming. *J. Clim.* **2010**, *23*, 4651–4668. [CrossRef]
42. Wang, Y.; Mingkui, C.A.O.; Bo, T.A.O.; Kerang, L.I. The characteristics of spatio-temporal patterns in precipitation in China under the background of global climate change. *Geogr. Res.* **2006**, *25*, 1031–1040.
43. Ding, Y.H.; Chan, J.C.L. The East Asian summer monsoon: An overview. *Meteorol. Atmos. Phys.* **2005**, *89*, 117–142.
44. Zhou, T.J.; Yu, R.C. Atmospheric water vapor transport associated with typical anomalous summer rainfall patterns in China. *J. Geophys. Res.* **2005**, *110*, D08104. [CrossRef]
45. IPCC. Climate Change 2013: The Physical Science Basis. In *Contribution of Working Group I to the Fifth Assessment Report of the Intergovernmental Panel on Climate Change*; Stocker, T.F., Qin, D., Plattner, G.-K., Tignor, M., Allen, S.K., Boschung, J., Nauels, A., Xia, Y., Bex, V., Midgley, P.M., Eds.; Cambridge University Press: Cambridge, UK; New York, NY, USA, 2013; Volume 15, pp. 1217–1308.
46. Yang, J.; Ding, Y.; Chen, R.; Liu, L. Variations of Precipitation and Evaporation in North China in Recent 40Years. *J. Arid Land Res. Environ.* **2003**, *17*, 6–11.
47. Comiso, J.C.; Hall, D.K. Climate trends in the Arctic as observed from space. *WIREs Clim. Chang.* **2014**, *5*, 389–409. [CrossRef] [PubMed]
48. Wu, F.; Li, W.; Li, W. Causes of Arctic Amplification: A Review. *Adv. Earth Sci.* **2019**, *34*, 232–242. [CrossRef]
49. Ma, S.M.; Zhu, C.W. Extreme Cold Wave over East Asia in January 2016: A Possible Response to the Larger Internal Atmospheric Variability Induced by Arctic Warming. *J. Clim.* **2019**, *32*, 1203–1216. [CrossRef]
50. Zhang, X.D.; Lu, C.H.; Guan, Z.Y. Weakened cyclones, intensified anticyclones and recent extreme cold winter weather events in Eurasia. *Environ. Res. Lett.* **2012**, *7*, 044044. [CrossRef]

51. Cane, M.A.; Clement, A.C.; Kaplan, A.; Kushnir, Y.; Pozdnyakov, D.; Seager, R.; Zebiak, S.E.; Murtugudde, R. Twentieth-Century Sea Surface Temperature Trends. *Science* **1997**, *275*, 957–960. [CrossRef]
52. Xia, Y.; Sun, X.; Yan, Y.; Feng, W.; Huang, F.; Yang, X.Q. Change of ENSO characteristics in response to global warming. *Chin. Sci. Bull.* **2017**, *62*, 1738–1751. [CrossRef]
53. Gill, A.E. Some simple solutions for heat-induced tropical circulation. *Quart. J. R. Met. Soc.* **1980**, *106*, 447–462. [CrossRef]
54. Kosaka, Y. Slow warming and the ocean see-saw. *Nat. Geosci.* **2018**, *11*, 12–13. [CrossRef]
55. IPCC. Climate Change 2001: The Scientific Basis. In *Contribution of Working Group I to the Third Assessment Report of the Intergovernmental Panel on Climate Change*; Houghton, J.T., Ding, Y., Griggs, D.J., Noguer, M., Linden, P.J., Dai, X., Maskell, K., Johnson, C.A., Eds.; Cambridge University Press: Cambridge, UK; New York, NY, USA, 2001; Volume 12, pp. 697–738.
56. Fang, C.; Wu, L.; Zhang, X. The impact of global warming on the pacific decadal oscillation and the possible mechanism. *Adv. Atmos. Sci.* **2013**, *31*, 118–130. [CrossRef]
57. Kattel, G.R.; Shang, W.X.; Wang, Z.J.; Langford, J. China's South-to-North Water Diversion Project Empowers Sustainable Water Resources System in the North. *Sustainability* **2019**, *11*, 3735. [CrossRef]
58. Liu, Y.; Wang, M.; Webber, M.; Zhou, C.T.; Zhang, W.J. Alternative water supply solutions: China's South-to-North-water-diversion in Jinan. *J. Environ. Manag.* **2020**, *276*, 111337. [CrossRef]